

This document is the unedited Author's version of a Submitted Work that was subsequently accepted for publication in ACS Appl. Energy Mater, copyright © American Chemical Society after peer review. To access the final edited and published work see <https://doi.org/10.1021/acsaem.3c02820>

Access to this work was provided by the University of Maryland, Baltimore County (UMBC) ScholarWorks@UMBC digital repository on the Maryland Shared Open Access (MD-SOAR) platform.

Please provide feedback

Please support the ScholarWorks@UMBC repository by emailing scholarworks-group@umbc.edu and telling us what having access to this work means to you and why it's important to you. Thank you.

Probing In Operando Manganese Dissolution and Associated Mechanical Deformation in LiMn_2O_4 Cathodes

Author Names: Lihong Zhao^a, Ömer Özgür Çapraz^{a,b}, Nancy R. Sottos^{a*}

^aDepartment of Material Science and Engineering, Beckman Institute for Advanced Science and Technology, University of Illinois at Urbana-Champaign, Champaign, 61801, USA

^bChemical, Biochemical and Environmental Engineering, The University of Maryland – Baltimore County, Baltimore, MD 21250

*Corresponding Author E-mail Address: n-sottos@illinois.edu

*Corresponding Author Postal Address: 1304 W Green St, Urbana, IL 61801

ABSTRACT

Mn dissolution has been an Achilles heel of cost-effective Mn-based transition metal oxide cathodes, such as spinel LiMn_2O_4 (LMO). The Mn dissolution leads to rapid capacity fade due to degradation in the cathode structure and formation of solid-electrolyte interface on anodes. Extensive ex-situ and chronical studies have unveiled that unfavorable cycling condition leads to manganese dissolution into the electrolyte, however, the mechanism behind the manganese dissolution remains under debate. Here, we report in operando Mn dissolution profile and its correlation with the electro-chemo-mechanical instabilities in LMO cathode. We carried out operando characterization of Mn ion concentration in the electrolyte via UV-vis spectroscopy and in operando strain measurement in the cathode using digital image correlation. Mn dissolution is accompanied by strain evolution in LMO induced by phase transition. Overdischarging further exacerbates the dissolution in successive cycles. Image analysis further tracks the distribution and transport of Mn species in the electrolyte during cycling. We foresee that in operando electro-chemo-mechanical techniques developed in this study can be applied to investigate transition metal dissolution in other battery cathodes.

KEYWORDS

Lithium manganese oxide, Mn dissolution, UV-vis spectroscopy, digital image correlation, Jahn-Teller distortion

1. Introduction

Lithium-ion batteries have become an indispensable part in the field of portable electronics and electric vehicles.^{1,2} In conventional Li-ion battery cathode materials, the presence of cobalt contributes to the elevated costs and environmental concerns associated with its extraction. Cobalt-free cathode has gathered interest in society in pursuit of cheaper and cleaner energy storage.³ LMO (LiMn_2O_4) is a promising cathode material for lithium-ion batteries due to its high working voltage, high capacity, high abundance, and environmental friendliness.^{4,5} Nonetheless, LMO suffers from rapid capacity fade due to severe chemical instabilities associated with manganese dissolution.^{6–11} The dissolution of Mn ions from the cathode results in active material loss and promotes ion deposition onto the anode, fostering the formation of unfavorable solid electrolyte interface (SEI).^{12–17} Although the phenomenon of dissolution was observed decades ago, a consensus on the underlying mechanism remains elusive.⁷ Manganese dissolution has been observed in various conditions, such as storage at elevated temperature,^{8,18} at full delithiation,⁹ at high electrolyte acidity,¹⁰ and at overdischarge state.^{6,19} When LMO undergoes overdischarge (over-lithiate), the Mn element undergoes reduction to a +3 valence state. This transition renders Mn(III) susceptible to the *Jahn-Teller* distortion phenomenon, leading to geometric distortions and a loss of degeneracy in its electronic state.^{7,20,21} Numerous studies have documented the rapid dissolution of LMO attributed to the *Jahn-Teller* effect.

To date, Mn dissolution studies are primarily based on *ex situ* techniques such as Inductively Coupled Plasma Mass Spectrometry (ICP-MS),^{19,22,23} X-Ray Fluorescence (XRF)^{16,19} and Electron Paramagnetic Resonance (EPR).²⁴ These measurements provide a quantitative Mn concentration profile in the electrolyte over cumulative cycles. *In situ* characterization of Mn ion concentration has been reported with microcapillary *in situ* sampling¹⁶ or rotating ring disk electrode (RRDE)

methods.¹¹ However, the microcapillary method has a limited sampling rate that does not allow real-time detection, and RRDE requires a high scanning rate that does not reveal detailed electrochemical information. Advancements in X-ray spectroscopy have recently enabled the visualization of Mn dissolution sites within the LMO cathode across different states of charge,²⁵ yet the real-time monitoring of Mn concentration within the electrolyte remains an ongoing challenge. Gaining a comprehensive Mn dissolution profile during electrochemical cycling would significantly enhance our understanding of this phenomenon. Previously we reported an electrochemically-stable UV-vis probe 4-(2-pyridylazo) resorcinol (PAR) that indicates the Mn ion concentration in the electrolyte and its potential for real-time dissolution characterization.²⁶

Here, we report a direct correlation between Mn dissolution and LMO phase transition through an innovative combination of operando techniques. Through high-throughput UV-vis spectroscopy, we performed real-time monitoring of Mn ion concentration in the electrolyte, providing insights into the dissolution phenomenon. Simultaneously, we measured the strain evolution in LMO cathode with Digital Image Correlation (DIC) to probe potential-dependent mechanical deformations in the cathode. By synchronizing in operando UV-vis spectroscopy with DIC measurements, we uncovered a compelling interplay between Mn dissolution and LMO phase transition, yielding a comprehensive understanding of their interconnected behaviors. We found Mn dissolution in LMO is accompanied by strain evolution induced by phase transition. Furthermore, overdischarging exacerbates the dissolution in successive cycling or immersion, as well as slows down the kinetics of Li intercalation. In addition, image analysis visualizes crosstalk phenomena in electrolyte, showcasing the transport of dissolved Mn towards the anode during discharge cycles. Our results provide insight to dissolution mechanisms in Mn-based cathode materials.

2. Materials and Methods

2.1. Sample Preparation

Neat electrolyte for electrochemical tests consists of 1 mol/L LiPF_6 (98 %) in ethylene carbonate (EC, Anhydrous, 99%) and dimethyl carbonate (DMC, Anhydrous, >99%) mixed at 1:1 (by volume). The electrolyte for Mn detection (Detection electrolyte) contains 10 mg/L (46 $\mu\text{mol/L}$) 4-(2-pyridylazo) resorcinol (PAR, 96%) as an indicator and 1 vol.% (23 mmol/L) phosphazene base (BTPP, tert-butylimino-tri(pyrrolidino)phosphorane) to ensure pH neutrality. Artificial Mn source manganese acetylacetonate $\text{Mn}(\text{acac})_2$ and $\text{Mn}(\text{acac})_3$ were used to calibrate UV-vis absorption intensity versus Mn ion concentration in the electrolyte. For the cathode preparation, LiMn_2O_4 (electrochemical grade), Super P carbon black (MTI), and polyvinylidene fluoride (PVdF, Kureha) were mixed and dissolved into N-methyl pyrrolidone (NMP) by 8:1:1:35 ratio. The mixture was homogenized at 8000 rpm for 1 hour into a slurry. The slurry was cast on 15 μm Al foil roughened with grit 600 sandpaper, and dried in ambient condition overnight, followed by vacuum-drying at 80 $^\circ\text{C}$ for 2 hours. The dried cathode film was tailored into a 1.5 cm \times 1.5 cm square, with 3.2 mg/cm^2 active material loading and ca. 0.47 mAh/cm^2 areal capacity. All chemicals were purchased from Sigma Aldrich if not specified.

2.2. Custom Cell for Operando UV-vis spectroscopy and image analysis

The customized cell for electrolyte spectroscopic analysis is shown in **Figure S1a-c**. The cell chamber comprised of polychlorotrifluoroethylene (Kel-F) was sealed with two pieces of quartz windows that allow light transmission. The LMO cathode was spot-welded to the top surface of a cubic stainless-steel current collector; and the Li metal anode (Alfa Aesar) was pressed onto a similar stainless-steel current collector with a rough top surface to enhance metal-to-metal

adhesion. The remaining surfaces of the cubic current collector were covered by polytetrafluoroethylene (PTFE, Teflon) to minimize its contact with electrolyte. The bottom surface of the electrode block was threaded at the center to allow an electric connection towards the exterior circuit, and the connection was sealed with an O-ring. Cathode and anode current collectors were assembled at two sides of the cell, facing each other with a distance between electrode surfaces to allow light transmission through the gap. The distance was set to 2.6 mm for spectroscopic analysis and 11.7 mm for image analysis. The light beam passed through the cell right beside the cathode, to enable instant detection of Mn ions upon dissolution.

2.3. Battery Cycling

The custom cell was first filled with neat electrolyte and cycled at C/10 between 3.0-4.3 V for one cycle. This formation cycle facilitates the electrolyte decomposition to form stable interphases and minimizes its impact on the current-voltage profile in later cycles. Then, the neat electrolyte was removed and replaced by the detection electrolyte, to characterize Mn dissolution in galvanostatic cycling. Three hours of resting was applied before electrochemical cycling to stabilize open-circuit voltage, as well as to avoid bubbles trapped in the cell chamber from blocking the light path. Cell was assembled in Ar-filled glovebox (MBraun) with H₂O and O₂ level below 1 ppm. High-powered tungsten halogen light source (Ocean optics, HL-2000-HP, 360-2400 nm) and high-throughput UV-vis detector (Ocean optics Q2000) were used to monitor the UV-vis absorption spectrum of the electrolyte during the cycling process. Imaging was performed with a color camera (Basler A602fc) and a planar light source. All electrochemical tests were performed with a battery cycler (Arbin, BT 2000). The electrochemical data were recorded every 10 seconds, while the UV-vis spectrum was collected every minute. Cyclic voltammetry was performed at 50 μ V/s without the initial formation cycle.

2.4. Strain Measurement

Cathode strain was measured with Digital Image Correlation (DIC) following a previously published experimental protocol.^{27–30} DIC is a full-field optical method, which correlates changes in the grayscale values of a surface speckle pattern to measure the deformation of the composite cathode. We used the natural speckle pattern of the composite electrode for DIC analysis. A CCD camera (EXi Aqua, Q-imaging) equipped with a 12X zoom lens (Navitar) was used to capture images of a 2.5 x 3.5 mm region of interest (ROI) on a scale of 3.24 $\mu\text{m}/\text{pixel}$. The commercial software VIC2D was used to calculate displacements and strains using a subset size of 60 μm by 60 μm . The in-plane strains due to free expansion and contraction of the electrode are nearly equal in the x and y directions and here we report only the normal strain in x direction, ϵ_{xx} .

2.5. Elemental Analysis of SEI

The mass of Mn deposited on Li metal anode was measured *ex situ* after the cycle. The Li metal anode (1.5 cm \times 1.5 cm) was dissolved in 15 mL of nano-pure water after cycling, and the amount of elemental Mn that has deposited on the Li metal anode was measured by ICP-MS (PerkinElmer – Models NexION 350D).

2.6. Image analysis

Images of the custom cell were recorded during electrochemical testing every minute using a color camera (Basler A602fc) with a 50-cm-focal-length lens. A tungsten light source was connected to a planer diffuser for background lighting. The diffuser provides a uniform transmitted illumination and separates the custom cell from the heat-generating light source. LabVIEW program was used to control the imaging process. All images were acquired at 20 ms exposure time and 350 dB gain to ensure that electrolyte color was identical over experiments.

3. Results and Discussion

3.1. Validation of the technique

We designed a custom cell to measure Mn concentration in the electrolyte during cycling (**Figure 1a**). In previous work, we reported the chelation of PAR with Mn ions and its characteristic absorption at 534 nm in UV-vis spectroscopy, as depicted in **Figure 1b**.²⁶ Deprotonated PAR chelates with Mn ion and changes its color from yellow to red (**Figure 1c**). The linear correlation between Mn ion concentration and normalized absorption peak intensity of electrolyte was verified in the custom cell setup with artificial Mn source Mn(acac)₂ (**Figure S1**). The absorption spectrum was normalized by deducting the absorption spectrum of PAR at 0 Mn concentration as the background spectrum. The normalized intensity of the characteristic absorption peak at 534 nm is plotted against the Mn ion concentration in the electrolyte in **Figure 1d**. When the PAR concentration was set to 46 μmol/L (10 mg/L), good linearity between absorption peak intensity and Mn ion concentration was observed below the detection limit of 40 μmol/L. Mn ion concentration in the custom cell during the cycling process was calculated by comparing the absorption intensity of the detection electrolyte with the calibration curve. The custom cell shows similar cycling performance as compared to coin cells (**Figure S1d**).

In this study, we replaced Proton Sponge (PS, 1,8-bis-(dimethylamino)naphthalene) reported in our previous work²⁶ and work reported by Sun et al.³¹ with a more stable proton scavenger BTPP. To assess the electrochemical stability, electrolytes containing PAR, PS, and BTPP were cycled with an inert electrode (Pt as cathode and Li metal as anode) between 3.5 V and 4.5 V for two cycles at 50 μV/s. Notably, both PAR and BTPP exhibited no discernible current response up to 4.5 V, while PS displayed an oxidation current at voltages exceeding 4.0 V (**Figure S2a**). Furthermore, the UV-vis spectra of electrolytes with PAR and BTPP remained consistent before

and after cycling, whereas the electrolyte with PS underwent a substantial color change (**Figure S2b**). The results affirm the electrochemical and spectroscopic stability of PAR and BTPP in our operando tests. Cyclic voltammogram shows no significant difference in LMO-Li cells with and without PAR-BTPP, as demonstrated in **Figure S2c**, suggesting a negligible impact on LMO cycling performance. The PAR-BTPP indicator is able to detect both Mn(II) and Mn(III). As shown in **Figure S3**, PAR-Mn(III) exhibits a gradual color change from skin color to pink over time, which we attribute to disproportionation in the electrochemical environment. We evaluated the chelation time between PAR-BTPP and Mn in **Figure S4**. Mn(acac)₂ solution was introduced to the electrolyte containing PAR-BTPP. The chelation occurred right after the addition of the Mn source, evidenced by the drastic change in the spectrum at t=1 minute. The absorption intensity at 534 nm stabilized after 25 minutes, indicating the equilibrium in the chelation reaction.

3.2. Tracking in operando Mn dissolution accompanied by electrochemical process

The LMO cathode was cycled via galvanostatic cycling between 3.0 and 4.3 V at C/10. The applied current, voltage response, and characteristic absorption intensity at the PAR-Mn characteristic peak are recorded over time (**Figure S5**). The open-circuit voltage of the custom cell stabilized after resting for three hours at around 3.3 V, which is consistent with the electrochemical potential of LMO vs. Li/Li⁺.⁵ Two voltage plateaus were observed at around 4.0 V and 4.15 V respectively, corresponding to two stages of delithiation in the spinel LMO.³² The absorption profile indicates the emergence of Mn dissolution as soon as the constant current is applied, and Mn concentration increases as delithiation/ lithiation proceeds.

The overall amount of Mn element in the electrolyte is calculated by multiplying custom cell volume (3.5 mL) and the Mn concentration (μmol/L) obtained from UV-vis absorption, with details listed in **Supplementary Note 1**. The degree of dissolution is defined as the ratio of

dissolved Mn (in mol) to the mole number of Mn in the LMO cathode. The amount of Mn dissolved into electrolyte within one galvanostatic cycle accounts for 0.099% of Mn in the LMO cathode. We also measured the amount of Mn deposited on Li metal anode using ICP-MS. After one cycle, Mn deposited on Li metal anode was 0.033 μmol , accounting for 0.041% of the Mn element in the cathode. The total degree of Mn loss from LMO is 0.140% per cycle. Choi et al. observed an overall 3.2% Mn dissolution from LMO after 50 cycles in a CR2032 coin cell, and an average degree of dissolution per cycle of approximately 0.064%.⁷ Esbenschade et al. immersed 0.2 g LMO powder in 15 mL electrolyte for 72 hours at room temperature and determined the Mn concentration in the electrolyte was 50 ppm through ICP-MS, which translates to 0.2 % of Mn in the cathode (calculated from reference ²³). Given the variation in experimental conditions, our operando detection technique is consistent with prior measurements of Mn concentration in electrolyte.

The differential capacity and UV-vis absorption were calculated as a function of cell potential (**Figure 2**). From the absorption profile, Mn dissolution only occurred between 3.9-4.3 V in both delithiation and lithiation cycles. This observation is consistent with the results reported from RRDE experiments.^{8,11} During both lithiation and delithiation, the two peaks in capacity derivative associated with the phase transition potentials of LMO correspond with the two peaks in absorption.^{19,28,32,33} These results indicate that LMO experiences the most rapid dissolution at the potential where LMO goes through substantial electrochemical reactions and phase transitions.

3.3. The Correlation between Mn dissolution with Electrochemical Strains in LMO

Strain generation in the LMO composite cathode was investigated to shed light on the correlation between Mn dissolution and electrochemical strain generation in the cathode.[30] The strain measurement was performed under the same condition with electrolyte containing PAR and BTPP.

Figure 3 shows the capacity derivative, strain, and strain derivative versus cell potential. A decrease in strain indicates shrinkage of electrode volume, which corresponds to lithium removal from the cathode during the delithiation process. Similarly, an increase in strain results from lithium intercalation into cathode during the lithiation process. The strain evolution well agrees with lattice parameter evolution in existing studies with operando synchrotron X-ray diffraction (XRD).³⁴ The two peaks in the strain derivatives are attributed to the volumetric changes induced during the phase transition. These peaks also align with the peak potentials in the capacity derivative. A similar correlation between potential-dependent capacity and strain was also observed in LMO without the UV-vis probe.²⁸ Interestingly, rapid Mn dissolution, significant strain accumulation, and peaks in differential capacity occur at the same potential, which confirms that Mn dissolution has a strong correlation with the phase transition of LMO during lithiation / delithiation process (**Figure S6**).

Phase transitions induce instability in the LMO spinel structure and lead to Mn dissolution. Choi et al. reported a positive correlation between Mn dissolution and change in LMO lattice parameters in both lithiation and delithiation processes.⁷ The formation of an unstable intermediate phase during LMO phase transitions was observed in electron energy-loss spectroscopy (EELS)²⁰ and operando synchrotron XRD,³⁴ and was claimed to be responsible for Mn dissolution. Phase transition also induces intra-particle heterogeneity in LMO that leads to crack formation and intensified Mn dissolution due to increased surface area exposed to the electrolyte.^{19,21,35,36} Instability of LMO structure during phase transitions results in rapid dissolution as observed in our in operando measurements.

Changes in LMO surface properties during phase transitions contribute to the Mn dissolution. Warburton et al. predicted a reduction in Mn content and generation of oxygen vacancy at LMO

surface during phase transitions via computational study.³³ Formation of soluble Mn_3O_4 at LMO surface during phase transitions was reported and proved to be responsible for Mn dissolution.^{34,37} Another research showed that electrolyte oxidation products above 4.2 V form metal complexes with surface Mn and accelerate dissolution.³⁸

3.3. Mn dissolution during Jahn-Teller Distortion

It has been widely reported that LMO undergoes massive dissolution due to *Jahn-Teller* distortion at overdischarge potential,⁵ when the valence of Mn decreases to +3. Mn(III) disproportionates to Mn(II) and Mn(IV), leading to the dissolution of Mn ions into the electrolyte.⁷ *In situ* X-ray reflectivity measurements show a 12% decrease in LMO cathode film thickness after five deep charge-discharge cycles between 2.5 V and 4.5 V.³⁴ Overdischarge leads to enhanced Mn dissolution over accumulative cycles; however, no direct experimental results are available to confirm that Mn ions are released into electrolyte at overdischarge potentials.

We compared the dissolution profile of LMO cathodes with and without overdischarge cycling. Cyclic voltammetry was performed on LMO cathodes between 2.5–3.5 V in the custom cell. During the overdischarge cycle (0-750 minutes), the LMO cathode does not exhibit intensified dissolution compared to the control test, where the LMO cathode is immersed in the electrolyte without cycling. However, in the long term (>2000 minutes), the LMO cathode with overdischarge cycling dissolves more Mn in the electrolyte (**Figure S7**) during immersion. We propose that overdischarge does not lead to immediate Mn dissolution, but may cause irreversible damage to the LMO structure,^{21,37} making it more susceptible to dissolution.

We further investigated the impact of overdischarge on Mn dissolution through operando characterization in **Figure 4**. Mn dissolution profile was measured between 3.5–4.5 V, with and

without an overdischarge cycle between 2.5–3.5 V. Here, we employed cyclic voltammetry instead of galvanostatic cycling to maintain a consistent experimental time within a specified voltage range (e.g. 3.5–4.5 V) for both cells. Additionally, PAR-BTPP was introduced at the onset of experiments to guarantee comparable Mn dissolution profiles in the initial cycle for both cells. As depicted in Figure 4, the two cells exhibited Mn dissolution levels of 9.1 and 9.5 $\mu\text{mol/L}$, respectively, in the first cycle. When LMO was cycled twice continuously within 3.5–4.5 V, Mn ion concentration increased throughout the test, but the amount of dissolution in the second cycle was less compared to the first cycle (**Figure 4a**). More dissolution in the first cycle possibly originates from additional electrochemical reactions in the formation process and the removal of LMO surface layer generated from cathode preparation.³⁴ When an overdischarge cycle (2.5–3.5 V) was conducted between two regular CV cycles (3.5–4.5 V), the LMO cathode experienced slow and steady dissolution within the overdischarge potential range, but much more Mn dissolved in the successive lithium intercalation process (**Figure 4b**). The cell with overdischarge history dissolved 16.5 $\mu\text{mol/L}$ in the second cycle, while the one without overdischarge dissolved 3.8 $\mu\text{mol/L}$. The dissolution profile of LMO during the second cycle (3.5–4.5 V) was directly compared with and without the overdischarge cycle in **Figure S8** for clarity. We observe more severe dissolution during the regular Li-ion intercalation process when LMO undergoes overdischarge in advance. We infer that LMO becomes vulnerable to Mn dissolution in chemical or electrochemical reactions after overdischarge, owing to the instability of LMO induced by *Jahn-Teller* distortion.

In **Figure 5**, the current and Mn concentration derivative were synchronized against voltage. The derivative of Mn dissolution within the standard voltage window (3.5–4.5 V, red curve) reveals two peaks that align precisely with current peaks observed in cyclic voltammetry. This

outcome effectively corroborates the galvanostatic results depicted in **Figure 2**, providing further evidence that the correlation between Mn dissolution and LMO phase transition remains consistent regardless of the cycling method employed. Once overdischarged, LMO exhibits a suppressed current response, severer dissolution, and certain hysteresis in the dissolution profile in the successive cycle, as depicted by the black curve. We considered the potential hysteresis in the dissolution profile arising from the chelation time of the PAR-Mn complex. As illustrated in **Figure S4**, both PAR and Mn achieve chelation equilibrium after 25 minutes, leading to a corresponding 75-mV shift in cyclic voltammetry at a scan rate of 50 $\mu\text{V/s}$. The potential impact of chelation time is depicted in **Figure S9**, where the solid line represents the dissolution profile in **Figure 5**, and the dashed line represents the scenario considering chelation time. The true dissolution profile is positioned between the solid and dashed lines.

Strain measurements also show that LMO cycled between 2.5–4.5 V exhibits reduced current response, suppressed strain rate, and lower overall strain compared to LMO cycled between 3.5–4.5 V (**Figure 6 and Figure S10**). The suppression can be attributed to the deteriorated LMO structure in the overdischarge, hindering Li intercalation into LMO. Such overdischarge-induced structural deterioration is also reported by Chen et al. through operando XRD.³⁴ The shift in strain peak indicates a hysteresis in electrode strain evolution, which suggests impeded kinetics of Li intercalation into LMO. The observation supports our hypothesis that *Jahn-Teller* distortion only affects LMO in the successive electrochemical process. Notably, the strain evolution observed in cyclic voltammetry (red curve) closely resembled the results from galvanostatic cycling in **Figure 3**. This similarity suggests that strain measurements exhibit minimal dependence on the chosen cycling method, similar to what we observed in LiFePO_4 composite electrodes.³⁹

3.4. Mn transports to anode during cycling

The spatial distribution of Mn within the electrolyte is further elucidated to provide insight into the interplay of dissolved species in LMO batteries. To achieve a more precise tracking of Mn-related species' spatial distribution, an optical cell featuring an extended electrode-to-electrode distance was utilized, as demonstrated in **Figure S11**. The characteristic absorption peak of the PAR-Mn complex at 534 nm corresponds to the red color in the image analysis. To quantitatively assess the degree of color alteration, the *Hue* value at each pixel was computed based on red (R), green (G), and blue (B) values using **Equations 1** and 2.⁴⁰ A calibration curve, depicted in **Figure S12**, was generated by manipulating the Mn concentration in the electrolyte using Mn(acac)₂. This curve displays a linear correlation between ΔHue and Mn concentration within the range of 0° to 45°. Through time- and space-resolved analysis of the ΔHue profile, the distribution of Mn within the electrolyte during the cycling process was characterized.

$$Hue = \arctan\left(\frac{\sqrt{3} \cdot (G-B)}{2R-G-B}\right) \quad (\text{Equation 1})$$

$$\Delta Hue = Hue|_{\text{initial}} - Hue|_t \text{ at each pixel} \quad (\text{Equation 2})$$

Image analysis was performed with large electrode separation (11.7 mm) to understand the temporal and spatial evolution of dissolved Mn concentration in the electrolyte during electrochemical cycling (**Figure 7a**). During the charging phase, Mn originating from LMO dissolved and accumulated around the cathode surface, as evidenced by minor changes in electrolyte color and ΔHue values (**Figures 7b-d** and **Supplementary Video 1**). Conversely, during the discharge cycle, Mn-related species migrated from the cathode toward the anode, as depicted in **Figures 7e-g**. This phenomenon is attributed to the electrostatic attraction between the negatively charged PAR-Mn complex and the charged electrode surfaces during cyclic voltammetry.

Further, when the voltage was held at 4.5 V at the end of the positive voltage scan and the current attenuated, the colored PAR-Mn species spontaneously moved toward the anode, as shown in **Figure S13** and **Supplementary Video 2**. At the initiation of the voltage hold (522 min), all the Mn dissolved during the delithiation process congregated near the cathode. This manifested as a dominant blue color in the ΔHue mapping, indicating low Mn concentration throughout the custom cell chamber. After approximately 4 hours of voltage hold (722 min), Mn departed away from the vicinity of the cathode surface, dispersing into the electrolyte. Interestingly, an accumulation of PAR-Mn complex near the Li metal anode was observed at this stage. We speculate that the PAR-Mn complex is drawn toward the anode to actively participate in the SEI formation process during Li plating.¹⁵ This phenomenon is in line with our ICP-MS observation that suggests the presence of residual Mn on the Li metal surface.

During the lithiation process (952 min), LMO goes through phase transitions from Cubic(III) back to Cubic(I), subsequently releasing a greater amount of Mn into the electrolyte, as indicated by drastic color change near the cathode surface. On the anode side, a thin Mn-deficient layer was observed near the Li metal anode. This observation is attributed to the removal of Mn-rich species, possibly in conjunction with the removal of pulverized SEI materials during the stripping process. Our experiments visualize the transport of Mn-containing species towards the anode during cycling, highlighting a plausible crosstalk scenario within the cell environment that influences SEI formation.¹² Notably, all characterizations in this article are performed in a “flooded cell” setup with sufficient electrolyte. This configuration facilitates Mn dissolution from LMO without regard to solubility limits, while the potential impact of Mn on SEI formation is likely minor, given the generally low Mn concentration. It is noteworthy that in practical batteries with lean electrolyte, the dissolved Mn may reach saturation, potentially curtailing further dissolution. On the other hand,

this scenario renders the anode more susceptible to non-ideal SEI formation, accentuating the challenges associated with crosstalk phenomena.

4. Summary

In this work, we demonstrated the correlation between Mn dissolution and strain evolution of LMO cathode using operando UV-vis spectroscopy and DIC measurements. The peaks in the differential absorption profile and differential capacity profile are well matched with each other, suggesting Mn dissolution from LMO is strongly correlated to the electrochemical reaction. Strain measurement also indicates Mn dissolution during lithium intercalation results from the phase transition of LMO. When LMO was subject to overdischarge at 2.5 V, it did not exhibit instant dissolution; however, enhanced dissolution was observed in successive chemical or electrochemical processes. *Jahn-Teller* distortion on Mn(III) at overdischarge potential leads to irreversible damage on LMO, which intensifies Mn dissolution. Image analysis shows the transport of dissolved Mn towards the anode during the discharge cycle, visualizing the well-known crosstalk mechanism that affects anode SEI formation.⁴¹

AUTHOR INFORMATION

Corresponding Author

*Nancy R. Sottos

Department of Material Science and Engineering, Beckman Institute for Advanced Science and Technology, University of Illinois at Urbana-Champaign, Champaign, 61801, USA

ORCID: 0000-0002-5818-520X; email: n-sottos@illinois.edu

Author

†Lihong Zhao

Department of Material Science and Engineering, Beckman Institute for Advanced Science and Technology, University of Illinois at Urbana-Champaign, Champaign, 61801, USA

†Current affiliation: Department of Electrical and Computer Engineering, Texas Center for Superconductivity at University of Houston, University of Houston, Houston, 77204, USA

ORCID: 0000-0003-2308-1053; email: lzhao26@cougarnet.uh.edu

†Ömer Özgür Çapraz

Department of Material Science and Engineering, Beckman Institute for Advanced Science and Technology, University of Illinois at Urbana-Champaign, Champaign, 61801, USA

†Current affiliation: Chemical, Biochemical and Environmental Engineering, The University of Maryland – Baltimore County, Baltimore, MD 21250, USA

ORCID: 0000-0002-2396-4748; email: capraz@umbc.edu

Author Contributions

Conceptualization: L.Z., Ö.Ö.C., and N.R.S.; investigation: L.Z. and Ö.Ö.C., writing: L.Z. and Ö.Ö.C.; supervision: N.R.S. funding acquisition: N.R.S.

Notes

The authors declare no competing financial interest.

Supporting Information

Custom cell components and experimental setup (Figure S1); Stability test of indicators (Figure S2); Evolution from Mn^{3+} to Mn^{2+} in indicator electrolyte (Figure S3); Chelation time between PAR-BTPP and Mn^{2+} (Figure S4); Potential, current, and Mn dissolution profile of LMO electrode (Figure S5); Correlation between differential capacity, strain derivative, and dissolution derivative of LMO (Figure S6); Mn dissolution profile of LMO after overdischarge cycle (Figure S7); The effect of the overdischarge cycle on Mn dissolution in successive lithium intercalation process (Figure S8); Mn concentration evolution of LMO in cyclic voltammetry considering PAR-Mn chelation time (Figure S9); Strain evolution of LMO with and without cycling in overdischarge window (Figure S10); Custom cell and setup for image analysis (Figure S11); Correlation between Mn concentration and *Hue* value (Figure S12); Mn concentration mapping during voltage hold (Figure S13); Calculation of dissolved Mn ratio (Supplementary Note 1); Electrochemical profile, raw image, and Hue analysis in cyclic voltammetry (Supplementary video 1) and in voltage-hold (Supplementary video 2).

Acknowledgments

This work was supported by the Center for Electrochemical Energy Science, an Energy Frontier Research Center funded by the U.S. Department of Energy, Office of Science, Basic Energy Sciences. The authors thank Beckman Institute for Advanced Science and Technology for the use of centralized research facilities. The authors thank Prof. Scott R. White for mentorship, inspiration and valuable insights into this project.

References

- (1) Lu, L.; Han, X.; Li, J.; Hua, J.; Ouyang, M. A Review on the Key Issues for Lithium-Ion Battery Management in Electric Vehicles. *J Power Sources* **2013**, *226*, 272–288. <https://doi.org/10.1016/j.jpowsour.2012.10.060>.
- (2) Yoo, H. D.; Markevich, E.; Salitra, G.; Sharon, D.; Aurbach, D. On the Challenge of Developing Advanced Technologies for Electrochemical Energy Storage and Conversion. *Mater. Today* **2014**, *17* (3), 110–121. <https://doi.org/10.1016/j.mattod.2014.02.014>.
- (3) Li, W.; Erickson, E. M.; Manthiram, A. High-Nickel Layered Oxide Cathodes for Lithium-Based Automotive Batteries. *Nat Energy* **2020**, *5* (1), 26–34. <https://doi.org/10.1038/s41560-019-0513-0>.
- (4) Gummow, R. J.; Kock, A. de; Thackeray, M. M. Improved Capacity Retention in Rechargeable 4 V Lithium/Lithium-Manganese Oxide (Spinel) Cells. *Solid State Ionics* **1994**, *69* (1), 59–67. [https://doi.org/10.1016/0167-2738\(94\)90450-2](https://doi.org/10.1016/0167-2738(94)90450-2).
- (5) Thackeray, M. M. Manganese Oxides for Lithium Batteries. *Prog Solid State Ch* **1997**, *25* (1–2), 1–71. [https://doi.org/10.1016/s0079-6786\(97\)81003-5](https://doi.org/10.1016/s0079-6786(97)81003-5).
- (6) Bhandari, A.; Bhattacharya, J. Review—Manganese Dissolution from Spinel Cathode: Few Unanswered Questions. *J Electrochem Soc* **2016**, *164* (2), A106–A127. <https://doi.org/10.1149/2.0101614jes>.
- (7) Choi, W.; Manthiram, A. Comparison of Metal Ion Dissolutions from Lithium Ion Battery Cathodes. *J Electrochem Soc* **2006**, *153* (9), A1760. <https://doi.org/10.1149/1.2219710>.
- (8) Jang, D. H. Dissolution of Spinel Oxides and Capacity Losses in 4 V Li/Li_xMn₂O₄ Cells. *J Electrochem Soc* **1996**, *143* (7), 2204. <https://doi.org/10.1149/1.1836981>.

- (9) Jang, D. H. Electrolyte Effects on Spinel Dissolution and Cathodic Capacity Losses in 4 V $\text{Li}/\text{Li}_x\text{Mn}_2\text{O}_4$ Rechargeable Cells. *J Electrochem Soc* **1997**, *144* (10), 3342. <https://doi.org/10.1149/1.1838016>.
- (10) Wohlfahrt-Mehrens, M.; Vogler, C.; Garche, J. Aging Mechanisms of Lithium Cathode Materials. *J Power Sources* **2004**, *127* (1–2), 58–64. <https://doi.org/10.1016/j.jpowsour.2003.09.034>.
- (11) Wang, L.-F.; Ou, C.-C.; Striebel, K. A.; Chen, J.-S. Study of Mn Dissolution from $\text{Li}_x\text{Mn}_2\text{O}_4$ Spinel Electrodes Using Rotating Ring-Disk Collection Experiments. *J Electrochem Soc* **2003**, *150* (7), A905. <https://doi.org/10.1149/1.1577543>.
- (12) Betz, J.; Brinkmann, J.; Nölle, R.; Lürenbaum, C.; Kolek, M.; Stan, M. C.; Winter, M.; Placke, T. Cross Talk between Transition Metal Cathode and Li Metal Anode: Unraveling Its Influence on the Deposition/Dissolution Behavior and Morphology of Lithium. *Adv Energy Mater* **2019**, *9* (21), 1900574. <https://doi.org/10.1002/aenm.201900574>.
- (13) Shin, H.; Park, J.; Sastry, A. M.; Lu, W. Degradation of the Solid Electrolyte Interphase Induced by the Deposition of Manganese Ions. *J Power Sources* **2015**, *284*, 416–427. <https://doi.org/10.1016/j.jpowsour.2015.03.039>.
- (14) Joshi, T.; Eom, K.; Yushin, G.; Fuller, T. F. Effects of Dissolved Transition Metals on the Electrochemical Performance and SEI Growth in Lithium-Ion Batteries. *J Electrochem Soc* **2014**, *161* (12), A1915–A1921. <https://doi.org/10.1149/2.0861412jes>.
- (15) Song, Y.; Wang, L.; Sheng, L.; Ren, D.; Liang, H.; Li, Y.; Wang, A.; Zhang, H.; Xu, H.; He, X. The Significance of Mitigating Crosstalk in Lithium-Ion Batteries: A Review. *Energ Environ Sci* **2023**, *16* (5), 1943–1963. <https://doi.org/10.1039/d3ee00441d>.
- (16) Terada, Y.; Nishiwaki, Y.; Nakai, I.; Nishikawa, F. Study of Mn Dissolution from LiMn_2O_4 Spinel Electrodes Using in Situ Total Reflection X-Ray Fluorescence Analysis and Fluorescence XAFS Technique. *J Power Sources* **2001**, *97*, 420–422. [https://doi.org/10.1016/s0378-7753\(01\)00741-8](https://doi.org/10.1016/s0378-7753(01)00741-8).
- (17) Knehr, K. W.; Hodson, T.; Bommier, C.; Davies, G.; Kim, A.; Steingart, D. A. Understanding Full-Cell Evolution and Non-Chemical Electrode Crosstalk of Li-Ion Batteries. *Joule* **2018**, *2* (6), 1146–1159. <https://doi.org/10.1016/j.joule.2018.03.016>.
- (18) Zhou, G.; Sun, X.; Li, Q.-H.; Wang, X.; Zhang, J.-N.; Yang, W.; Yu, X.; Xiao, R.; Li, H. Mn Ion Dissolution Mechanism for Lithium-Ion Battery with LiMn_2O_4 Cathode: In Situ Ultraviolet–Visible Spectroscopy and Ab Initio Molecular Dynamics Simulations. *J. Phys. Chem. Lett.* **2020**, *11* (8), 3051–3057. <https://doi.org/10.1021/acs.jpcllett.0c00936>.
- (19) Liu, T.; Dai, A.; Lu, J.; Yuan, Y.; Xiao, Y.; Yu, L.; Li, M.; Gim, J.; Ma, L.; Liu, J.; Zhan, C.; Li, L.; Zheng, J.; Ren, Y.; Wu, T.; Shahbazian-Yassar, R.; Wen, J.; Pan, F.; Amine, K. Correlation between Manganese Dissolution and Dynamic Phase Stability in Spinel-Based

Lithium-Ion Battery. *Nat Commun* **2019**, *10* (1), 4721. <https://doi.org/10.1038/s41467-019-12626-3>.

(20) Leifer, N.; Schipper, F.; Erickson, E. M.; Ghanty, C.; Talianker, M.; Grinblat, J.; Julien, C. M.; Markovsky, B.; Aurbach, D. Studies of Spinel-to-Layered Structural Transformations in LiMn_2O_4 Electrodes Charged to High Voltages. *J Phys Chem C* **2017**, *121* (17), 9120–9130. <https://doi.org/10.1021/acs.jpcc.7b00929>.

(21) Ben, L.; Yu, H.; Chen, B.; Chen, Y.; Gong, Y.; Yang, X.; Gu, L.; Huang, X. Unusual Spinel-to-Layered Transformation in LiMn_2O_4 Cathode Explained by Electrochemical and Thermal Stability Investigation. *ACS Appl Mater Inter* **2017**, *9* (40), 35463–35475. <https://doi.org/10.1021/acsami.7b11303>.

(22) Tang, D.; Ben, L.; Sun, Y.; Chen, B.; Yang, Z.; Gu, L.; Huang, X. Electrochemical Behavior and Surface Structural Change of LiMn_2O_4 Charged to 5.1 V. *J Mater Chem A* **2014**, *2* (35), 14519–14527. <https://doi.org/10.1039/c4ta02109f>.

(23) Esbensen, J. L.; Fox, M. D.; Gewirth, A. A. LiMn_2O_4 @Au Particles as Cathodes for Li-Ion Batteries. *J Electrochem Soc* **2014**, *162* (1), A26–A29. <https://doi.org/10.1149/2.0241501jes>.

(24) Shilina, Y.; Ziv, B.; Meir, A.; Banerjee, A.; Ruthstein, S.; Luski, S.; Aurbach, D.; Halalay, I. C. Combined Electron Paramagnetic Resonance and Atomic Absorption Spectroscopy/Inductively Coupled Plasma Analysis As Diagnostics for Soluble Manganese Species from Mn-Based Positive Electrode Materials in Li-Ion Cells. *Anal Chem* **2016**, *88* (8), 4440–4447. <https://doi.org/10.1021/acs.analchem.6b00204>.

(25) Zhang, Y.; Hu, A.; Xia, D.; Hwang, S.; Sainio, S.; Nordlund, D.; Michel, F. M.; Moore, R. B.; Li, L.; Lin, F. Operando Characterization and Regulation of Metal Dissolution and Redeposition Dynamics near Battery Electrode Surface. *Nat Nanotechnol* **2023**, 1–8. <https://doi.org/10.1038/s41565-023-01367-6>.

(26) Zhao, L.; Chénard, E.; Çapraz, Ö. Ö.; Sottos, N. R.; White, S. R. Direct Detection of Manganese Ions in Organic Electrolyte by UV-Vis Spectroscopy. *J Electrochem Soc* **2018**, *165* (2), A345–A348. <https://doi.org/10.1149/2.1111802jes>.

(27) Çapraz, Ö. Ö.; Bassett, K. L.; Gewirth, A. A.; Sottos, N. R. Electrochemical Stiffness Changes in Lithium Manganese Oxide Electrodes. *Adv Energy Mater* **2017**, *7* (7), 1601778. <https://doi.org/10.1002/aenm.201601778>.

(28) Çapraz, Ö. Ö.; Rajput, S.; White, S.; Sottos, N. R. Strain Evolution in Lithium Manganese Oxide Electrodes. *Exp Mech* **2018**, *58* (4), 561–571. <https://doi.org/10.1007/s11340-018-0381-8>.

(29) Tavassol, H.; Jones, E. M. C.; Sottos, N. R.; Gewirth, A. A. Electrochemical Stiffness in Lithium-Ion Batteries. *Nat Mater* **2016**, *15* (11), 1182–1187. <https://doi.org/10.1038/nmat4708>.

- (30) Jones, E. M. C.; Silberstein, M. N.; White, S. R.; Sottos, N. R. In Situ Measurements of Strains in Composite Battery Electrodes during Electrochemical Cycling. *Exp Mech* **2014**, *54* (6), 971–985. <https://doi.org/10.1007/s11340-014-9873-3>.
- (31) Sun, X.; Xiao, R.; Yu, X.; Li, H. Screening LiMn₂O₄ Surface Modification Schemes under Theoretical Guidance. *ACS Appl. Mater. Interfaces* **2022**, *14* (8), 10353–10362. <https://doi.org/10.1021/acsami.1c23478>.
- (32) Warburton, R. E.; Iddir, H.; Curtiss, L. A.; Greeley, J. Thermodynamic Stability of Low- and High-Index Spinel LiMn₂O₄ Surface Terminations. *ACS Appl Mater Inter* **2016**, *8* (17), 11108–11121. <https://doi.org/10.1021/acsami.6b01069>.
- (33) Gao, P.; Ishikawa, R.; Tochigi, E.; Kumamoto, A.; Shibata, N.; Ikuhara, Y. Atomic-Scale Tracking of a Phase Transition from Spinel to Rocksalt in Lithium Manganese Oxide. *Chem Mater* **2017**, *29* (3), 1006–1013. <https://doi.org/10.1021/acs.chemmater.6b03659>.
- (34) Chen, X.; Vörös, M.; Garcia, J. C.; Fister, T. T.; Buchholz, D. B.; Franklin, J.; Du, Y.; Droubay, T. C.; Feng, Z.; Iddir, H.; Curtiss, L. A.; Bedzyk, M. J.; Fenter, P. Strain-Driven Mn-Reorganization in Overlithiated LiMn₂O₄ Epitaxial Thin-Film Electrodes. *ACS Appl Energy Mater* **2018**, *1* (6), 2526–2535. <https://doi.org/10.1021/acsaem.8b00270>.
- (35) Finegan, D. P.; Vamvakeros, A.; Tan, C.; Heenan, T. M. M.; Daemi, S. R.; Seitzman, N.; Michiel, M. D.; Jacques, S.; Beale, A. M.; Brett, D. J. L.; Shearing, P. R.; Smith, K. Spatial Quantification of Dynamic Inter and Intra Particle Crystallographic Heterogeneities within Lithium Ion Electrodes. *Nat Commun* **2020**, *11* (1), 631. <https://doi.org/10.1038/s41467-020-14467-x>.
- (36) Su, L.; Choi, P.; Nakamura, N.; Charalambous, H.; Litster, S.; Ilavsky, J.; Reeja-Jayan, B. Multiscale Operando X-Ray Investigations Provide Insights into Electro-Chemo-Mechanical Behavior of Lithium Intercalation Cathodes. *Appl. Energy* **2021**, *299*, 117315. <https://doi.org/10.1016/j.apenergy.2021.117315>.
- (37) Lin, M.; Ben, L.; Sun, Y.; Wang, H.; Yang, Z.; Gu, L.; Yu, X.; Yang, X.-Q.; Zhao, H.; Yu, R.; Armand, M.; Huang, X. Insight into the Atomic Structure of High-Voltage Spinel LiNi_{0.5}Mn_{1.5}O₄ Cathode Material in the First Cycle. *Chem Mater* **2017**, *29* (1), 292–303. <https://doi.org/10.1021/cm503972a>.
- (38) Jarry, A.; Gottis, S.; Yu, Y.-S.; Roque-Rosell, J.; Kim, C.; Cabana, J.; Kerr, J.; Kostecki, R. The Formation Mechanism of Fluorescent Metal Complexes at the Li_xNi_{0.5}Mn_{1.5}O_{4-δ}/Carbonate Ester Electrolyte Interface. *J Am Chem Soc* **2015**, *137* (10), 3533–3539. <https://doi.org/10.1021/ja5116698>.
- (39) Özdöğru, B.; Dykes, H.; Padwal, S.; Harimkar, S.; Çapraz, Ö. Ö. Electrochemical Strain Evolution in Iron Phosphate Composite Cathodes during Lithium and Sodium Ion Intercalation. *Electrochimica Acta* **2020**, *353*, 136594. <https://doi.org/10.1016/j.electacta.2020.136594>.

- (40) Kamiyama, M.; Taguchi, A. Color Conversion Formula with Saturation Correction from HSI Color Space to RGB Color Space. *IEICE Trans. Fundam. Electron., Commun. Comput. Sci.* **2021**, *E104.A* (7), 1000–1005. <https://doi.org/10.1587/transfun.2020eal2087>.
- (41) Zhao, L. Self-reporting of Mn ion dissolution and self-stabilization of cathode-electrolyte interface in lithium ion batteries. Ph.D. Dissertation, University of Illinois at Urbana Champaign, Champaign, IL, **2020**.

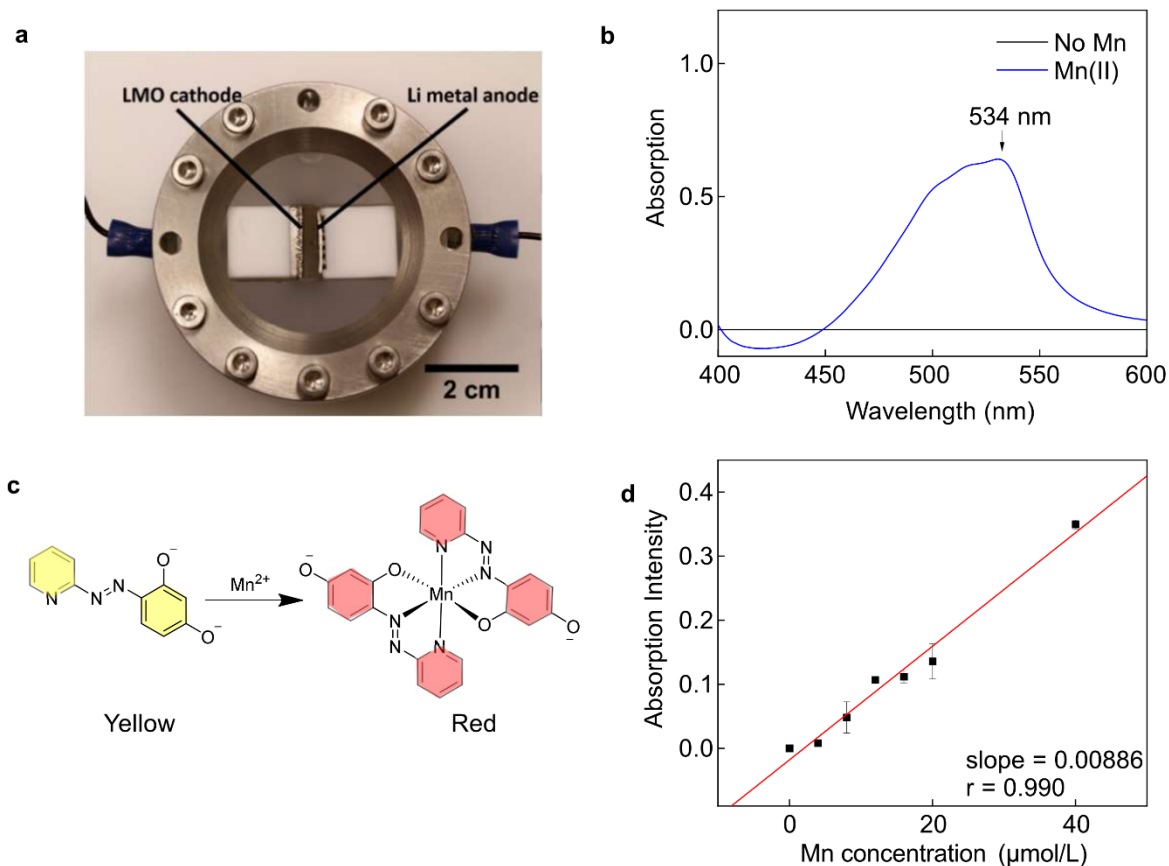


Figure 1. Custom cell setup for spectroscopic analysis. (a) Custom cell to measure Mn concentration in the electrolyte during cycling. (b) Characteristic peak of PAR-Mn complex at 534 nm. (c) Proposed color changing mechanism of PAR indicator. (d) Calibration curve of Mn concentration with respect to absorption intensity.

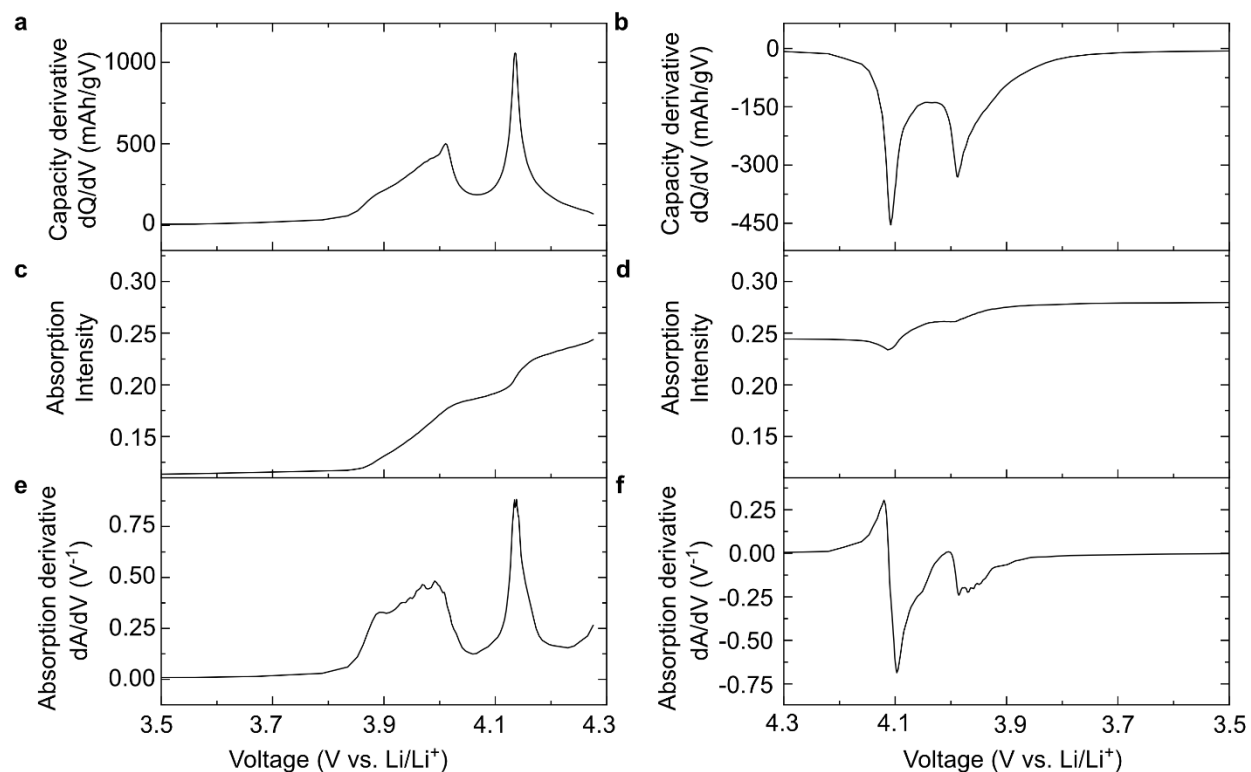


Figure 2. Differential capacity, absorption, and differential absorption of LMO. The plot shows the 2nd cycle profile at 0.1 C. Capacity derivative in (a) charge and (b) discharge cycle. Absorption intensity in (c) charge and (d) discharge cycle. Absorption intensity represents Mn concentration in the electrolyte. dA/dV profile represents absorption intensity derivative versus voltage. The locations of two peaks in the dQ/dV profile are well aligned with peaks in dA/dV, suggesting a strong correlation between electrochemical reactions and Mn dissolution.

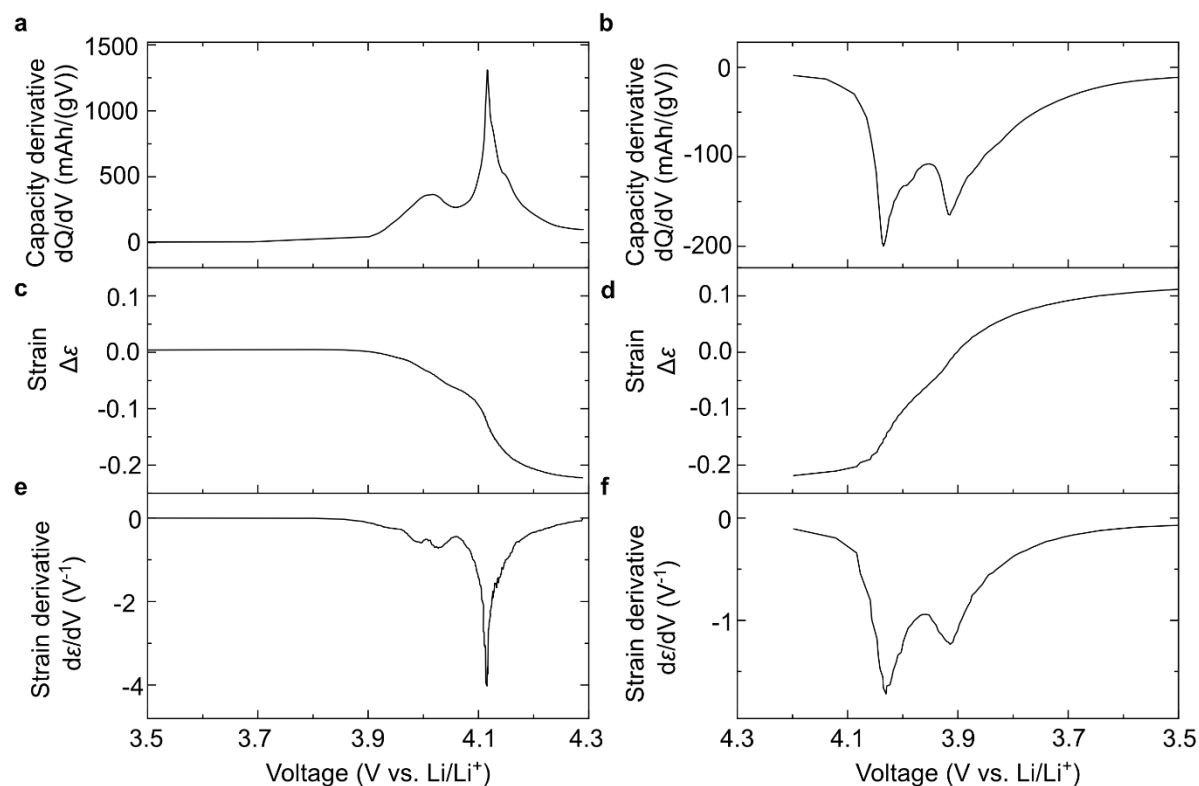


Figure 3. Correlation between differential capacity, strain evolution, and strain derivative of LMO. The plot shows the 2nd cycle profile at 0.1 C. Capacity derivative in (a) charge and (b) discharge cycle. Strain in (c) charge and (d) discharge cycle. Strain derivative in (e) charge and (f) discharge cycle. Peaks in strain derivative correspond to dramatic volume change induced by phase transitions in LMO, which well aligns with peaks in the dQ/dV profile.

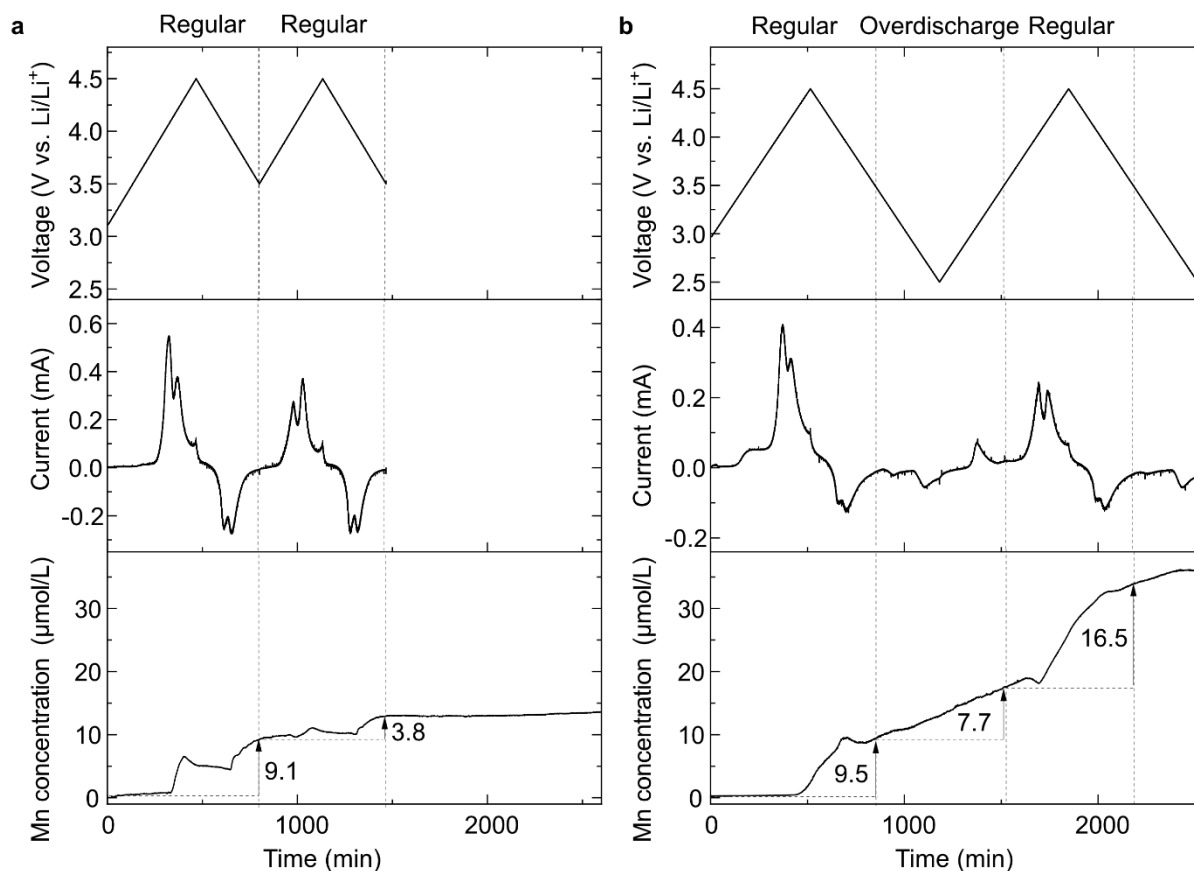


Figure 4. The effect of the overdischarge cycle on Mn dissolution in successive lithium intercalation process. Mn concentration profile between 3.5–4.5 V, (a) without and (b) with overdischarge cycle between 2.5–3.5 V. Severe Mn dissolution was observed after the overdischarge cycle. The dissolution profile in the second *Regular* cycle is plotted in Figure S7 for direct comparison. CV scan is carried out at 50 $\mu\text{V/s}$.

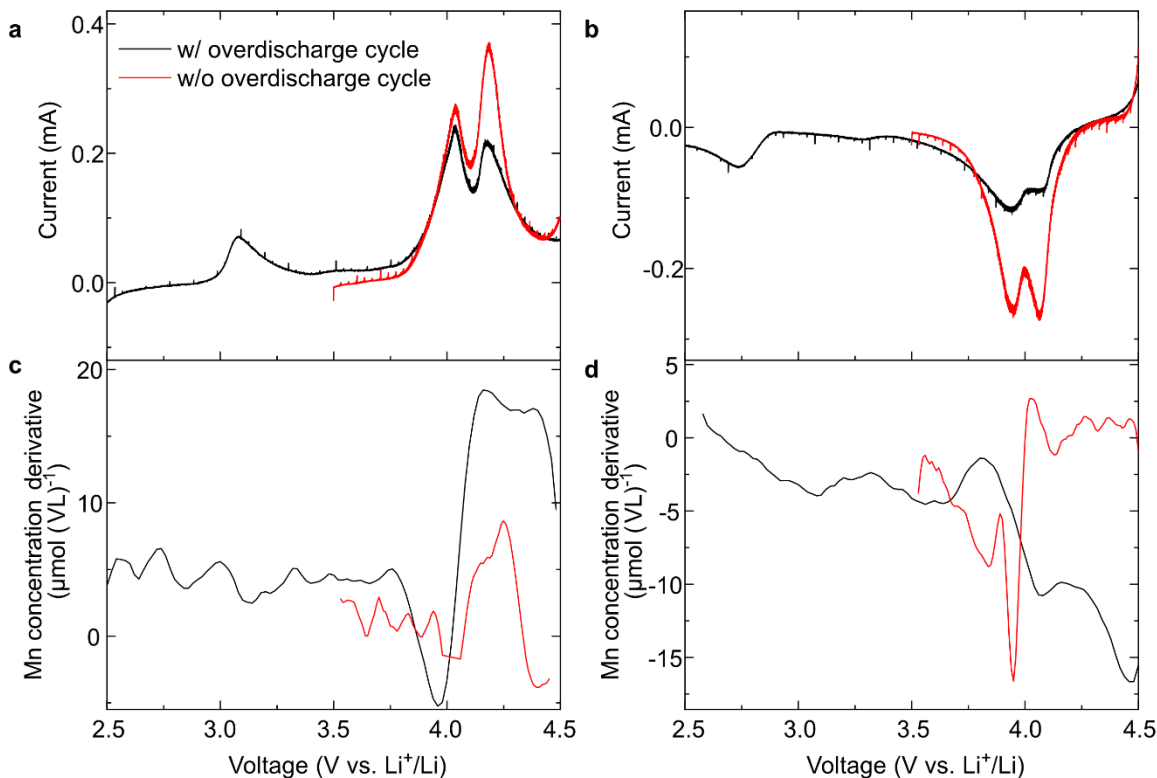


Figure 5. Mn concentration evolution of LMO with and without cycling in overdischarge window in cyclic voltammetry at 50 $\mu\text{V/s}$. Current response in (a) anodic and (b) cathodic scan. Mn concentration derivative in (c) anodic scan and (d) cathodic scan. The Mn concentration derivative is calculated from the dissolution profile in the second cycle with cyclic voltammetry experiment (Figure 4). LMO cycled between 2.5–4.5 V (*black curve*) demonstrates suppressed current response and dissolution compared to LMO cycled between 3.5–4.5 V (*red curve*). The dissolution profile of 3.5–4.5 V sample (*red curve*) aligned well with absorption derivative in Figure 2. *Jahn-Teller* distortion during the overdischarge window (2.5–3.5 V) facilitates Mn dissolution in successive cycles.

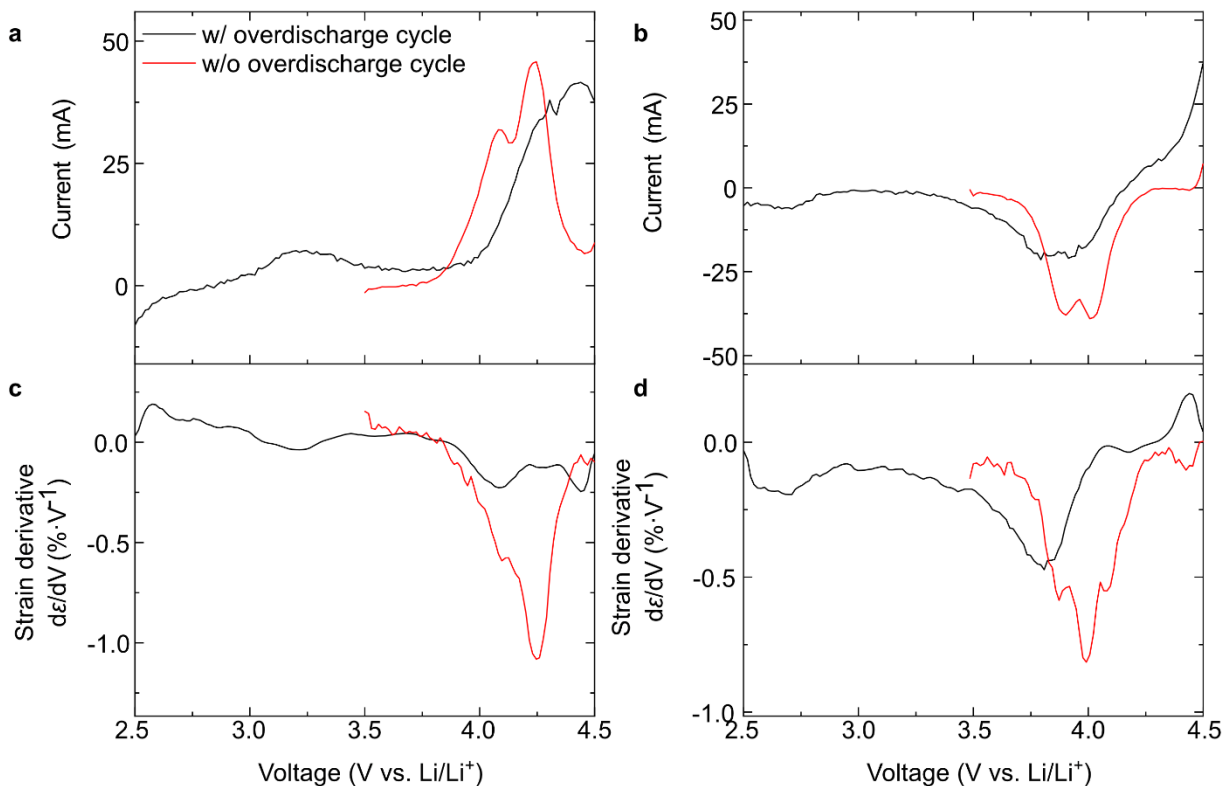


Figure 6. Strain evolution of LMO with and without cycling in overdischarge window in cyclic voltammetry at 50 $\mu\text{V/s}$. Current response in (a) anodic and (b) cathodic scan. Strain derivative in (c) anodic scan and (d) cathodic scan. LMO cycled between 2.5–4.5 V (*black curve*) demonstrates suppressed current response and strain rate compared to LMO cycled between 3.5–4.5 V (*red curve*). *Jahn-Teller* distortion during the overdischarge window (2.5–3.5 V) deteriorates the structure of LMO and influences the successive electrochemical process.

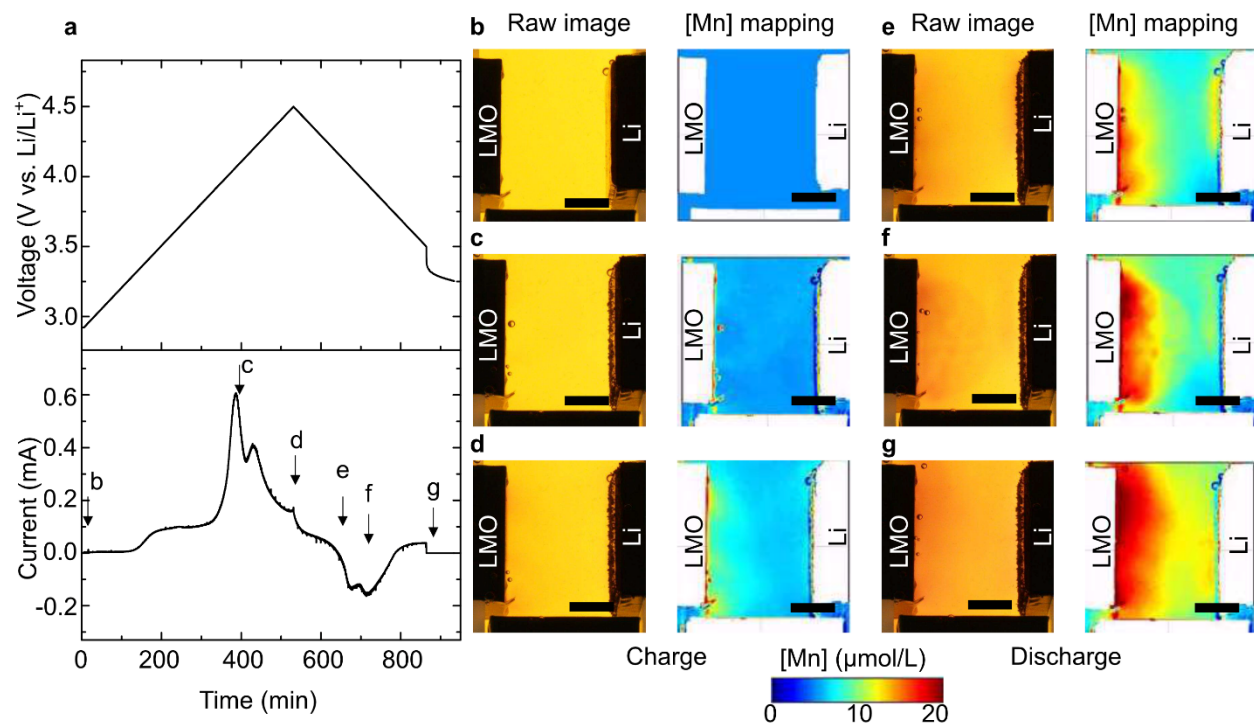


Figure 7. Mn mapping in the electrolyte during cyclic voltammetry at 50 $\mu\text{V/s}$. (a) Cyclic voltammogram of LMO in imaging setup. Raw image and corresponding Mn concentration ([Mn]) mapping derived from ΔHue analysis at (b) 0 min, (c) 427 min, (d) 509 min, (e) 624 min, (f) 710 min, (g) 902 min. The scale bar is 5 mm.

ToC

